SLAC-PUB-8848
BABAR-PROC-01/14
hep-ex/0106043
June, 2001

Charmless B Decays from *BABAR* ($B^0 \to K^{*0}\gamma$ and $B^0 \to \pi^+\pi^-, K^+\pi^-, K^+K^-$)

M. Convery
Stanford Linear Accelerator Center
Stanford University, Stanford, CA 94309
(for the *BABAR* Collaboration)

Abstract

The BaBar experiment has completed its first year of data-taking during which 21 fb^{-1} of data were accumulated. We present preliminary results on two types of charmless B decays based on this data sample. The first, $B^0 \to K^{*0}\gamma$, is a so-called electromagnetic penguin. And the second, $B^0 \to h^+h^{'-}$, where $h^{(')}$ can be either a pion or kaon, can come from either penguin diagrams or Cabibbo suppressed tree diagrams.

Contributed to the Proceedings of the XV Rencontres de Physique de La Vallée d'Aoste,
March 4–10, 2001, La Thuile, Italy.

Stanford Linear Accelerator Center, Stanford University, Stanford, CA 94309

Work supported in part by Department of Energy contract DE-AC03-76SF00515.

1 Theory and Motivation

In the Standard Model, the charmless B decays that will be discussed in this paper proceed via the Feynman diagrams shown in Figure 1. The diagram shown in Figure 1(a) is the "penguin" diagram. This diagram has a loop with a u-type quark, which can emit either a Z^0, a photon (γ), or a gluon (g) before recombining to form either d or s quark. Due to its heavy mass, the diagram containing a top quark is much larger than those containing u or c quarks, which can thus be ignored. Therefore, there are CKM factors of V_{ts} or V_{td} at the recombination vertex, depending on whether the final state contains an s or d quark. If the boson emitted in the quark-loop is a photon, then final states such as $B^0 \to K^{*0}\gamma$ [1] (with an s-quark in the final state) and $B^0 \to \rho^0\gamma$ (with a d-quark in the final state) can be produced. If the emitted boson is a gluon, then fully hadronic states such as $B^0 \to K^+\pi^-$ can be produced. Neither diagrams containing Z^0 bosons, nor those with d-quarks have yet been observed.

Measuring decays produced by the penguin diagram is interesting because it can potentially give a low energy window on high energy phenomena. For example, in the Standard Model, measuring the branching ratio of $B^0 \to \rho^0\gamma$ will give information about the value of V_{td}. Beyond the standard model, a charged Higgs (H^+) or similar particle could replace the W and either enhance the branching ratio for $B^0 \to K^{*0}\gamma$ or lead to direct CP violation [1].

The "tree diagram" of Figure 1(b) can lead to the decay $B^0 \to \pi^+\pi^-$. This is especially interesting, because the final state is a CP-eigenstate and the decay has a Matrix Element that is proportional to the the CKM factor V_{ub}. This means that the decay could be used to measure time-dependent CP violation. Such a measurement, when combined with constraints from isospin conservation, could yield a very clean measurement of the unitarity angle α, which is difficult to measure in any other way [2]. However, the penguin diagram can also produce the same final state and, since it has a different matrix element, could complicate the measurement. Regardless, a precise measurement of α will require higher statistics than are currently available.

In this paper, we will present results on analyses of the decay modes $B^0 \to K^{*0}\gamma$ and decays to two light charged hadrons ($B^0 \to \pi^+\pi^-, K^+\pi^-, K^+K^-$), which we will often call $B^0 \to h^+h'^-$. Preliminary BABAR results on charmless decays based on about half of the current data set have been presented in [3] ($B^0 \to h^+h'^-$) and in [4] ($B^0 \to K^{*0}\gamma$). Here, we present updated preliminary results based on the full data-set of the first year.

2 The PEP-II B Factory

The data that will be described in this paper was taken with the BABAR detector at the PEP-II B Factory, which is at located the Stanford Linear Accelerator Center (SLAC) and has been running since May of 1999. PEP-II is an asymmetric e^+e^- collider that collides a beam of e^-'s with an energy 9.0 GeV with a beam of e^+'s with an energy of 3.1 GeV. This produces a center of mass energy of equal to the $\Upsilon(4s)$ mass and thus provides a copious source of B mesons. The peak luminosity achieved in "Run 1", which stretched from November of 1999 to October of 2000, was $3.3 \times 10^{33}\text{cm}^{-2}\text{sec}{-1}$. The integrated luminosity collected during that time was approximately 21 fb^{-1}, which is equivalent to $(22.7 \pm 0.4) \times 10^6$ $B\bar{B}$ pairs. Additionally, 3 fb^{-1} of data was taken at energies below the $\Upsilon(4s)$ peak.

The asymmetric energies of the PEP-II beams are required for doing the time-dependent CP asymmetries that are the heart of the BABAR physics program [5]. However, they cause

[1] Charge conjugation is assumed throughout this paper unless specifically stated.

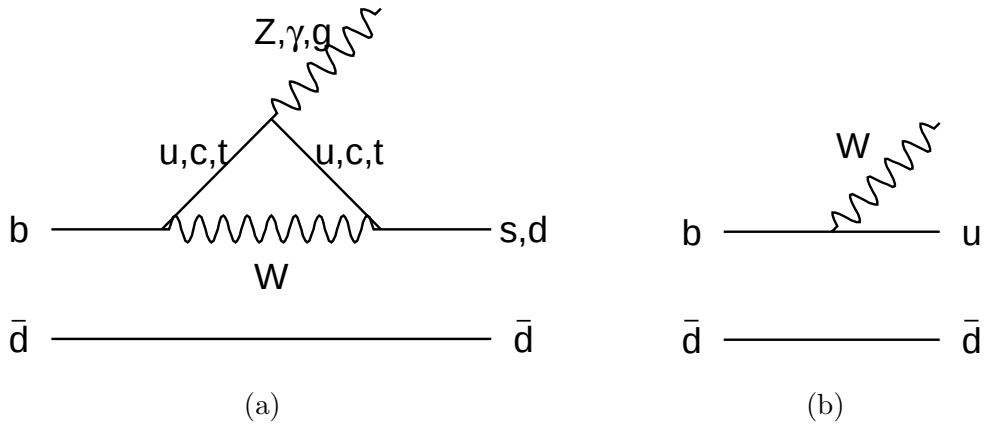

Figure 1: *Feynman diagrams responsible for charmless B decays. (a) is the "penguin" diagram, which contributes to the all of the final states being discussed in this paper. (b) is the "tree" diagram, which can contribute to the* $B^0 \to \pi^+\pi^-$ *decay.*

some problems for the measurement of charmless branching ratios. For example, the range of momenta of the daughters produced in two-body B decays is rather narrow in the center of mass frame ($2.4\,\mathrm{GeV} < p_{2-body,CMS} < 2.8\,\mathrm{GeV}$). In the lab frame, however, the range is wider ($2\,\mathrm{GeV} < p_{2body,lab} < 4\,\mathrm{GeV}$). This means, for example, that the the particle identification device used to separate π's from K's needs to work over a wider range of momenta than it would otherwise.

3 The BABAR Detector

Figure 2 shows a schematic of the BABAR detector. The innermost component of BABAR is 5 layer Silicon Vertex Tracker. Outside of that is a 40 layer central Drift Chamber. The DIRC (Detector of Internally Reflected Cherenkov light) [6], which is used for charged hadron identification is composed of two parts: the quartz radiator bars, which are located just outside of the Drift Chamber, and the array of Photo Multiplier tubes, which is located on the backward side of detector outside the central region. Surrounding the DIRC radiator bars is an electromagnetic calorimeter using CsI crystals. Outside of this is the Superconducting Solenoid, which provides a 1.5 T field. Finally, the solenoid is surrounded by an iron flux return, which has gaps instrumented with resistive plate chambers to provide muon and neutral hadron identification. The capabilities of BABAR are described in more detail in [5]. Since the charged hadron identification provided by the DIRC is key to both of the analyses described in this note, we will describe it in more detail here.

4 The DIRC

Figure 3 shows the principle of DIRC operation. As charged particles pass through the radiator bars, Cherenkov light is produced. A fraction of that light is trapped inside the rectangular bars by total internal reflection. As the light than propagates down the length of the bar, typically

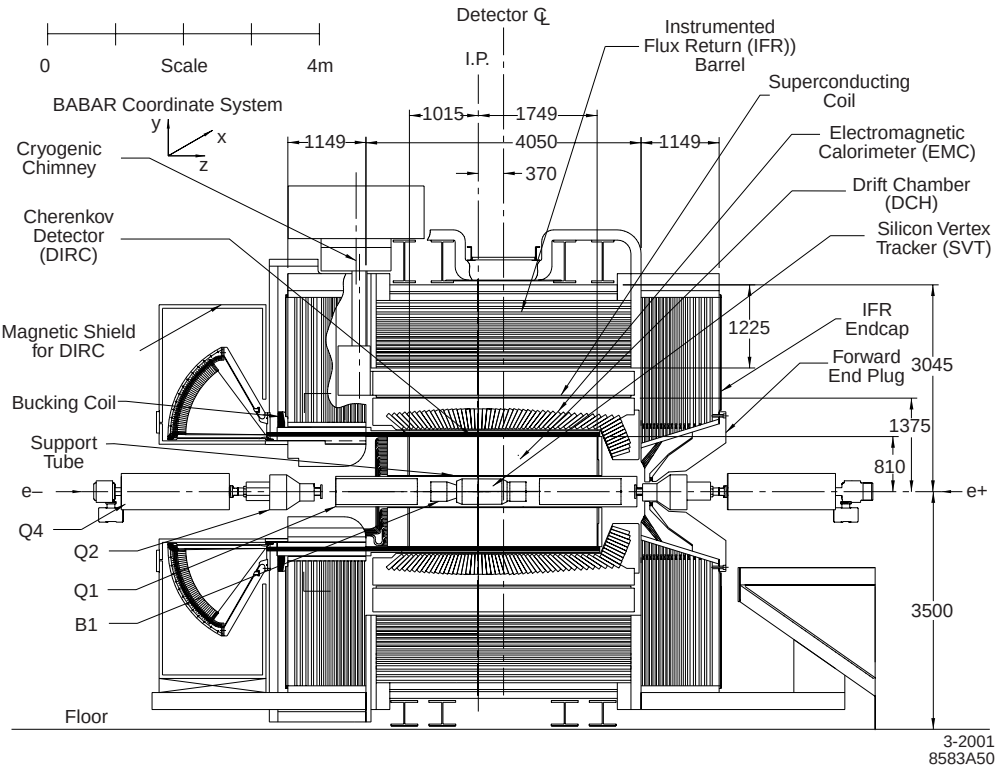

Figure 2: *Side view of the BABAR detector.*

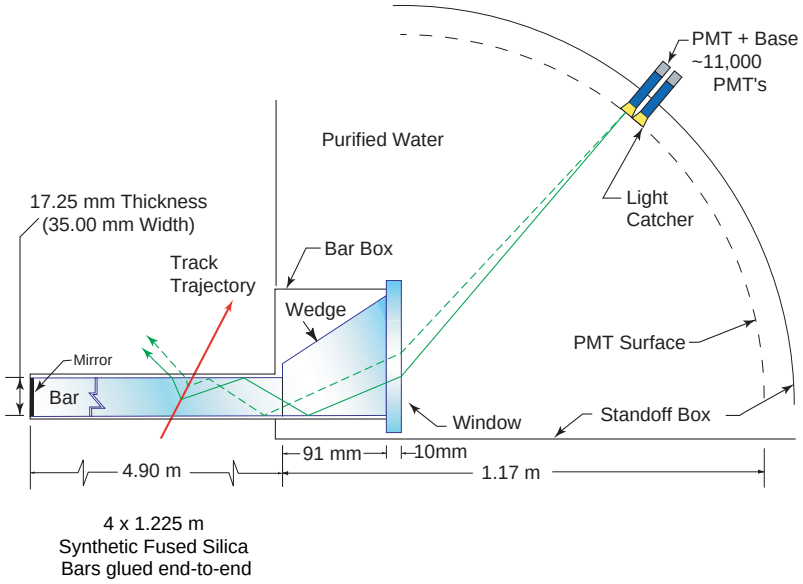

Figure 3: *The principle of DIRC operation. See text for explanation.*

bouncing 200 times, the Cherenkov pattern is preserved, up to reflection ambiguities. At the end of the bar, the light emerges into a stand-off region where the Cherenkov pattern is allowed to expand before being detected by an array of roughly 11,000 phototubes.

Measurement of the Cherenkov angle of the detected light provides excellent π, K separation. The performance of the DIRC can be checked using samples of π's and K's identified in $D^{*+} \to \pi^+ D^0 (D^0 \to K^- \pi^+)$. Figure 4(a) shows the performance of a K selection algorithm based on the DIRC Cherenkov angle measurement on these samples. The efficiency for correctly identifying K's is roughly 90%, while the probability of mis-identifying a π as K is roughly 2 % at low momentum, but degrades somewhat at high (> 2.5GeV) momentum. Figure 4(b) shows the bands of Cherenkov angles measured by the DIRC for high momentum tracks. The bands grow closer together at high momentum, but the separation is still better than 2.5 σ at 4 GeV, which is the kinematic limit for two-body B decays.

5 Analysis Procedure

A very similar procedure is used for both the $B^0 \to K^{*0}\gamma$ and $B^0 \to h^+ h^{'-}$ analyses. The first step is to compose "B candidates" of the desired final state out of the available charged tracks, photons and π^0's. Then, background is rejected based on event shape variables. Background levels are measured using off-resonance data or sideband regions of on-resonance data. To determine the number of signal events, a fit is performed to a set of kinematic variables. The signal efficiency is calculated in Monte Carlo, including adjustments for tracking efficiency and other related effects.

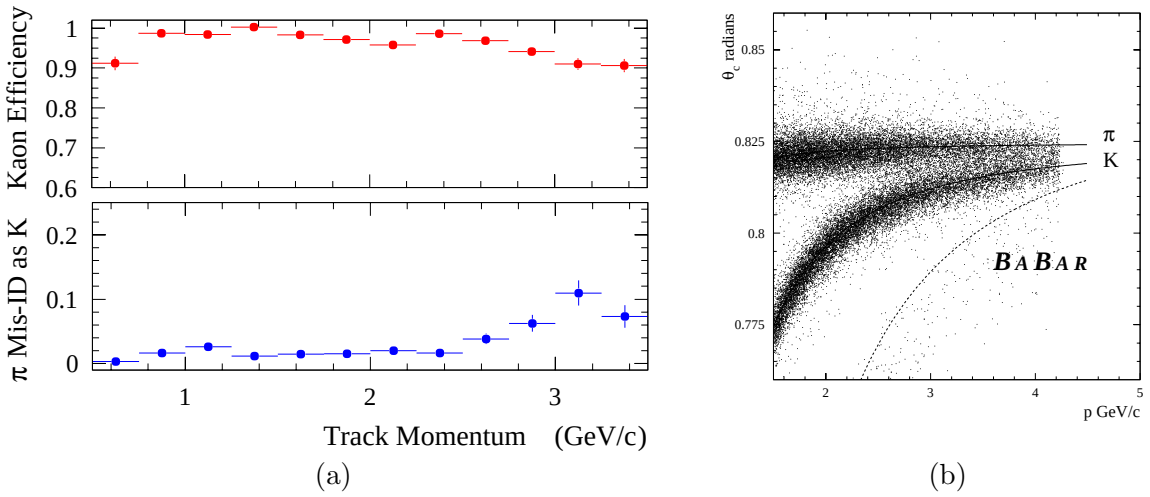

Figure 4: *π/K separation of the DIRC. a) shows the performance of a kaon selection algorithm using DIRC information. b) shows the raw Cherenkov angle measurement for samples of π's and K's.*

6 Background Suppression

Because the cross-section for continuum light-quark production is much higher than that for $B\bar{B}$ production $\sigma(e^+e^- \to q\bar{q}) \approx 3\sigma(e^+e^- \to B\bar{B})$ and because the tracks coming from continuum events tend to have higher momentum, the background to charmless decays comes mostly from continuum events. This background may be suppressed by noting that in the center of mass frame, continuum events are more "jetty" than the more spherical $B\bar{B}$ events.

The first step in this procedure is to define the "axis" of the candidate B-decay. In the case of $B^0 \to K^{*0}\gamma$, this is taken to be the direction of the photon. While for the case of $B^0 \to h^+h'^-$, it is taken as the thrust axis of the B candidate. Then, the tracks and neutral energy of the the remainder of the event (excluding the B candidate) are examined. In the case of $B^0 \to K^{*0}\gamma$ the thrust axis of the remainder is calculated and the angle between it and the candidate axis is called θ_t. Figure 5(a) shows the distribution of the $\cos\theta_t$ for signal and background. As expected for the "jetty" background, $\cos\theta_t$ is peaked toward 1. For the more spherical $B\bar{B}$ events, it has a flat distribution.

In the case of $B^0 \to h^+h'^-$ a more sophisticated approach, which was originally developed by CLEO is used [7]. This method defines a set of 9 concentric cones centered on the candidate axis. Each cone subtends 10° of solid angle and is folded to combine the forward and backward intervals. The energy in the ith cone is called x_i and a "Fisher Discriminant", F, is defined as

$$F = \sum_{i=1}^{9} \alpha_i x_i. \tag{1}$$

The coefficients α_i are varied so as to maximize the separation between signal and background. Figure 5(b) shows histograms of this quantity for signal and background.

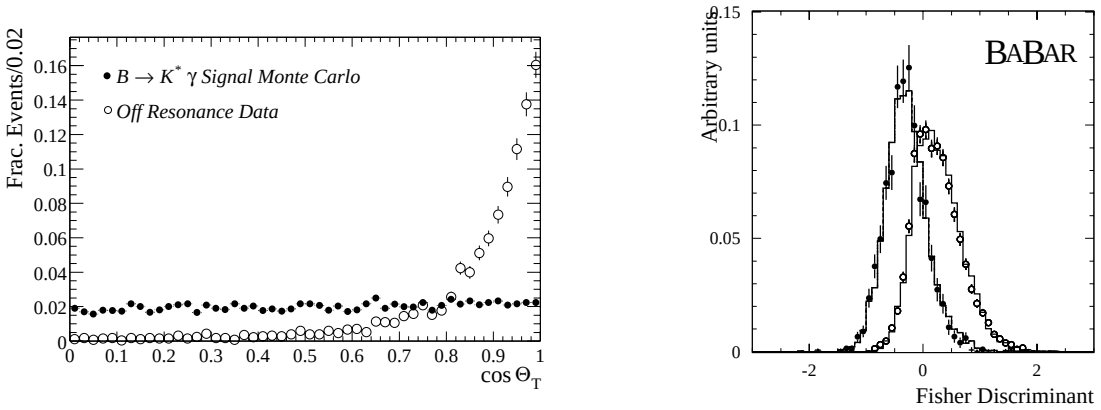

(a) (b)

Figure 5: *Event shape variables used for background suppression. a) shows the* $\cos\theta_t$ *variable used in* $B^0 \to K^{*0}\gamma$*. b) shows the Fisher Discriminant used in* $B^0 \to h^+h^{'-}$*. Solid circles are for signal, open circles for background.*

7 Kinematic Variables

Two kinematic variables are traditionally used in exclusive B-reconstruction in symmetric colliders operating at the $\Upsilon(4s)$. The first, known as the "beam-constrained mass" is defined as,

$$m_B \equiv \sqrt{E_{beam}^2 - p_B^2}, \tag{2}$$

where E_{beam} is the beam energy and p_B is the momentum of the B candidate in the center of mass system. Since the beam energy is precisely known, this variable has much better mass resolution than would be achieved by using the measured energy of the B candidate. The second variable is defined as

$$\Delta E \equiv E_B - E_{beam}, \tag{3}$$

where E_B is the measured energy of the B candidate. In the case of $B^0 \to h^+h^{'-}$, if one assumes that both daughters have the pion mass, then ΔE will peak at zero for signal events for which both daughters are pions. If one or more of the daughters are not pions, then the peak will be shifted away from zero, thus providing particle identification. In the case of $B^0 \to K^{*0}\gamma$, where there is no ambiguity in the particle masses, one expects a peak at zero.

In an asymmetric collider, one can simply boost the track parameters back into the center of mass frame and calculate m_B as usual. However, this requires assignment of masses to each of the particles. In some analyses, such as $B^0 \to h^+h^{'-}$, this is undesirable and can lead to worse m_B resolution if the wrong mass assignment is made. In such cases, it is desirable to define a new variable called the energy-substituted mass m_{ES},

$$m_{ES} \equiv \sqrt{(\frac{1}{2}s + \vec{p_0} \cdot \vec{p_B})/E_0^2 - p_B^2}, \tag{4}$$

where $\sqrt{s}$ is the center of mass energy, $\vec{p_0}$ and E_0 are the three-momentum and energy of the $\Upsilon(4s)$ and $\vec{p_B}$ is the three-momentum of the B candidate. This variable has the advantage that it uses

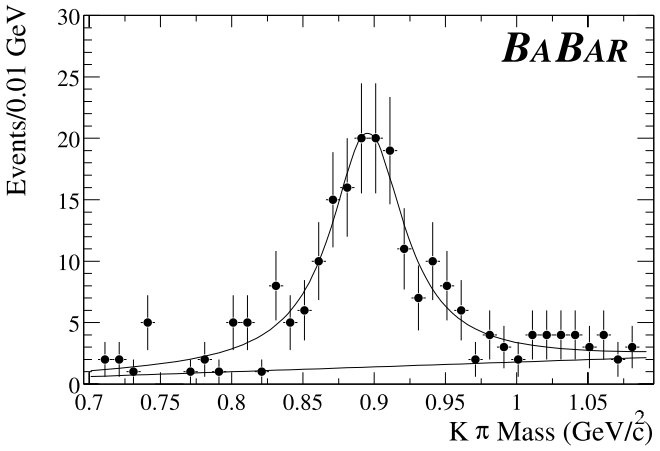

Figure 6: K^{*0} *mass peak for the final* $B^0 \to K^{*0}\gamma$ *sample.*

only quantities measured in the lab system, and thus requires no mass assignments to be made. It is identical to m_B if the lab and center of mass frames coincide. It is also equivalent to m_B if there is no ambiguity in the particle masses. A new version of ΔE is also defined,

$$\Delta E^* \equiv E_B^* - \sqrt{s}/2, \tag{5}$$

which also has shifts for different daughter masses.

8 $B^0 \to K^{*0}\gamma$ Analysis

8.1 $B^0 \to K^{*0}\gamma$ Candidates

The $B^0 \to K^{*0}\gamma$ decay is searched for in the mode $K^{*0} \to K^{\pm}\pi^{\mp}$. $B^0 \to K^{*0}\gamma$ decay candidates are composed out of available photons and K^{*0}'s, which are in turn composed of $K^{\pm}$'s and $\pi^{\mp}$'s.

In order to be considered, the photon candidate must be located cleanly within the active region of the calorimeter ($-0.73 < \cos\theta_{lab} < 0.9$) and must have an energy close to that expected in the center of mass ($2.3\,\mathrm{GeV} < E_{\gamma,CMS} < 2.8\,\mathrm{GeV}$). In addition, the photon must not be consistent with having come from a π^0 or η decay. Two cuts are applied to insure this. The transverse shape of the shower is used to reject those π^0's for which the two photons are not spatially separated. And, to reject π^0's and η's that do form two separate calorimeter clusters, the candidate photon is matched up with all other photons in the event and rejected if any of them gives a mass consistent with m_{π^0} or m_η. The efficiency of these photons cuts is 77%.

Similarly, the K^{*0} candidate must pass a number of cuts. First, the K^+ and π^- candidates must pass DIRC particle identification cuts. Then, the mass of the $K\pi$ system must be consistent with the K^{*0} ($0.796\mathrm{GeV} < m_{K\pi} < 0.996\mathrm{GeV}$). Finally, the helicity angle, defined as the angle between the K^+ direction in the K^* rest frame and the K^* flight direction, must satisfy $|\cos\theta_{hel}| < 0.75$. The efficiency of the K^{*0} cuts is 56 %. Figure 6 shows the K^{*0} mass peak in the final $B^0 \to K^{*0}\gamma$ sample.

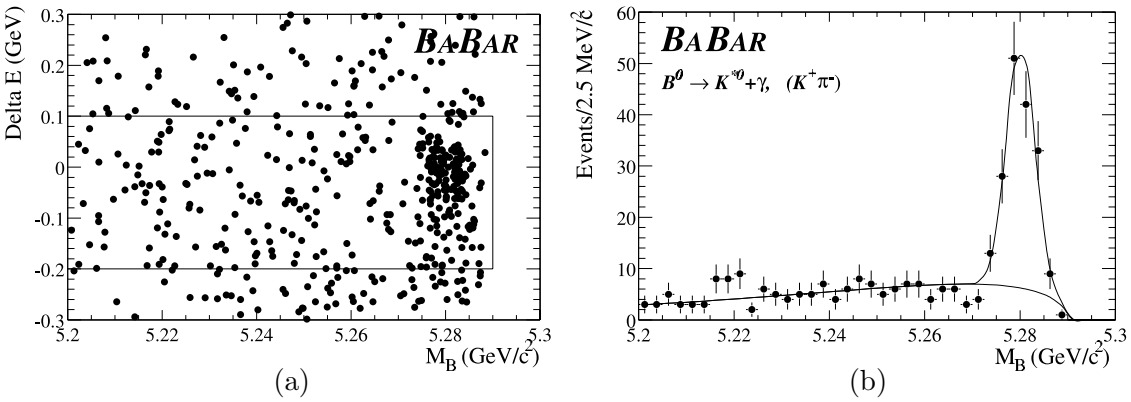

Figure 7: *The final sample of the $B^0 \to K^{*0}\gamma$ search. a) is a scatter plot of ΔE vs. m_B. b) is a projection onto the m_B axis, showing a clear $B^0 \to K^{*0}\gamma$signal.*

8.2 $B^0 \to K^{*0}\gamma$ Mass Fit

Once the photon and K^{*0} candidates have been identified, B candidates are formed from them. These candidates must pass a number of cuts in order to be considered in the final sample. The ΔE^* of the candidate, defined in Equation 5 must pass a cut of $-200MeV < \Delta E^* < 100MeV$. The "thrust angle" must pass the cut $|\cos\theta_t| < 0.8$. And finally, the polar angle of the B candidate in the center of mass frame must pass the cut $|\cos\theta_B^*| < 0.75$. The events that pass these cuts are shown in Figure 7(a) and (b). The concentration of events near $\Delta E^* = 0$ and $M_B = 5.28$ in Figure 7(a) indicates a strong $B^0 \to K^{*0}\gamma$ signal. In order to determine the number of signal events, a fit is performed on the M_B distribution. As shown in Figure 7(b), he background is modeled with an "Argus" function, whose shape is determined using data taken off the $\Upsilon(4s)$ resonance. The shape of the signal is Gaussian, and the mean, σ and amplitude are floated in the fit. The number of signal $B^0 \to K^{*0}\gamma$ events extracted from the fit is $N_{sig} = 139.2 \pm 13.1$.

8.3 $B^0 \to K^{*0}\gamma$ Results

The efficiency for observing a $B^0 \to K^{*0}\gamma$ event is calculated in Monte Carlo. This includes corrections for known differences between data and Monte Carlo for tracking efficiency, photon detection efficiency and particle identification efficiency. The efficiency is found to be $\epsilon = 0.209 \pm 0.013$, where the error is purely systematic. One can then use this efficiency to calculate the branching ratio as:

$$BR(B^0 \to K^{*0}\gamma) = \frac{N_{sig}}{N_{B\bar{B}} \times \epsilon \times B_{K^*}}, \tag{6}$$

where $N_{B\bar{B}}$ is the number of $B\bar{B}$ pairs in the sample, and B_{K^*} is the branching ratio for $K^{*0} \to K^-\pi^+$. The systematic error comes mostly from data-derived efficiency corrections. The preliminary result for the branching ratio is then:

$$BR(B^0 \to K^{*0}\gamma) = (4.39 \pm 0.41_{stat} \pm 0.27_{syst}) \times 10^{-5} \tag{7}$$

Measurement of a possible CP asymmetry in this decays is also of interest. The asymmetry is

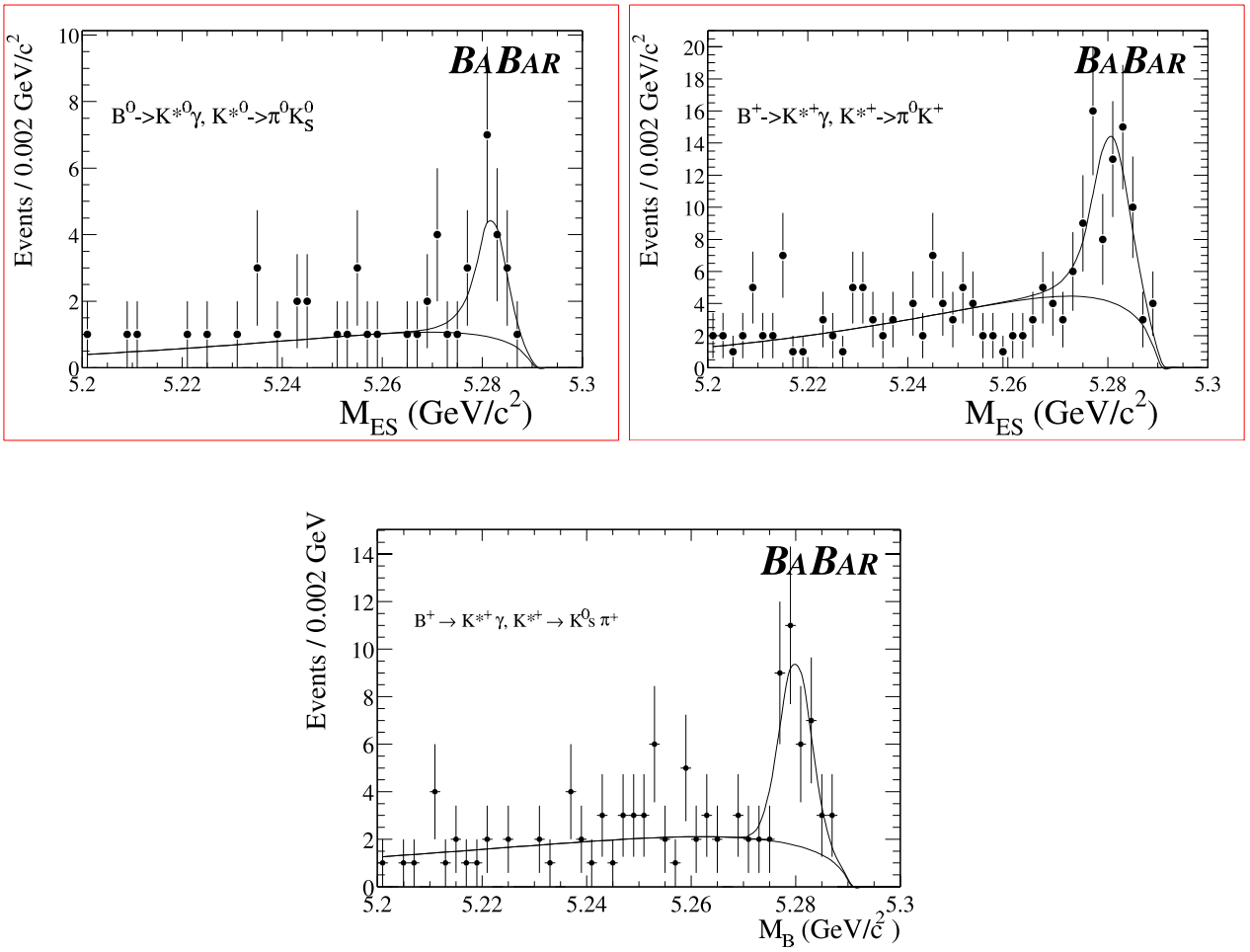

Figure 8: *Signals for three other modes of* $B \to K^*\gamma$.

defined as:

$$A_{CP} = \frac{N(\bar{B^0} \to \bar{K^{*0}}\gamma) - N(B^0 \to K^{*0}\gamma)}{N(\bar{B^0} \to \bar{K^{*0}}\gamma) + N(B^0 \to K^{*0}\gamma}) \tag{8}$$

Many of the systematic errors of the branching ratio measurement cancel out in this measurement and we are left with a preliminary measurement of:

$$A_{CP} = -0.035 \pm 0.094 \pm 0.022 \tag{9}$$

8.4 Other $B^0 \to K^{*0}\gamma$ Modes

Figure 8 shows evidence for three other modes of $B \to K^*\gamma$: $B^0 \to K^{*0}\gamma, K^{*0} \to \pi^0 K^0_s$; $B^+ \to K^{*+}\gamma, K^{*+} \to K^+\pi^0$; $B^+ \to K^{*+}\gamma, K^{*+} \to K^0_s\pi^+$. Although clear signals are evident in each of these modes, their efficiencies and systematic errors have not yet been fully evaluated. For this reason, no branching ratios or asymmetries will be presented for them at this time.

Variable	Definition
m_{ES}	Energy substituted B Mass, described in Section 7
ΔE	Energy difference, described in Section 7
F	Fisher discriminant output, described in Section 6
$\theta_{C,+}$	DIRC Cherenkov Angle for positive track
$\theta_{C,-}$	DIRC Cherenkov Angle for negative track

Table 1: *Variables used in the Maximum Likelihood fit of $B^0 \to h^+h'^-$ and their definitions.*

9 Analysis of $B^0 \to h^+h'^-$

9.1 $B^0 \to h^+h'^-$Candidates

$B^0 \to h^+h'^-$candidates are composed out of pairs of oppositely signed charged tracks, both of which must pass tracking quality cuts and DIRC quality cuts. The candidates must pass a cut on the "sphericity angle" which is almost identical to the "thrust angle", θ_t defined in Section 6, of $\cos\theta_s < 0.9$. Furthermore, the candidate events must pass cuts on the second Fox-Wolfram moment of $R_2 < 0.95$ and on sphericity of $S > 0.01$. Finally, loose cuts are placed on the kinematic variables of the decay: $5.2\,\mathrm{GeV} < m_{ES} < 5.3\,\mathrm{GeV}$ and $-0.15\,\mathrm{GeV} < \Delta E < 0.15\,\mathrm{GeV}$. In Monte Carlo, these cuts are found to have an efficiency of $\epsilon \approx 0.45$ for the $B^0 \to \pi^+\pi^-$mode. The 26404 events that pass these cuts in the data sample are put into a Maximum Likelihood fit described in the next section.

9.2 $B^0 \to h^+h'^-$Likelihood Fit

Since a small number of signal events are expected in the $B^0 \to h^+h'^-$modes, it is desirable to use a Maximum Likelihood fitting technique, rather than the more traditional "cut-and-count" technique. For the purposes of the fit, each event is considered to come from one of eight hypotheses: a true $B^0 \to \pi^+\pi^-$ event, a true $B^0 \to K^+\pi^-$ event (or charge conjugate), a true $B^0 \to K^+K^-$ event, a background $B^0 \to \pi^+\pi^-$ event, a background $B^0 \to K^+\pi^-$ event (or charge conjugate), or a background $B^0 \to K^+K^-$ event. The parameters that are varied in the the likelihood fit are the number of events in each of these hypotheses. The event variables that are fit to are listed in Table 1.

The likelihood function is defined as follows. A probability distribution function (PDF) is calculated for each event and hypothesis. It has the form:

$$P^{hypo}_{event} = P^{hypo}_{M_{ES}} P^{hypo}_{\Delta E} P^{hypo}_{F} P^{hypo}_{\theta_{C,+}} P^{hypo}_{\theta_{C,-}}, \tag{10}$$

where the P's are the PDF's for each variable given an event hypothesis. Typically, these are parameterized in terms of simple functions. The full likelihood function is then written,

$$\mathcal{L} = exp(-\sum_{hypo} N_{hypo}) \prod_{j=1}^{N} [\sum_{hypo} N_{hypo} P^{hypo}_{event}], \tag{11}$$

where N_{hypo} is the number of events in each hypothesis and N is the total nmber of events in the sample. This function is then maximized using standard tools.

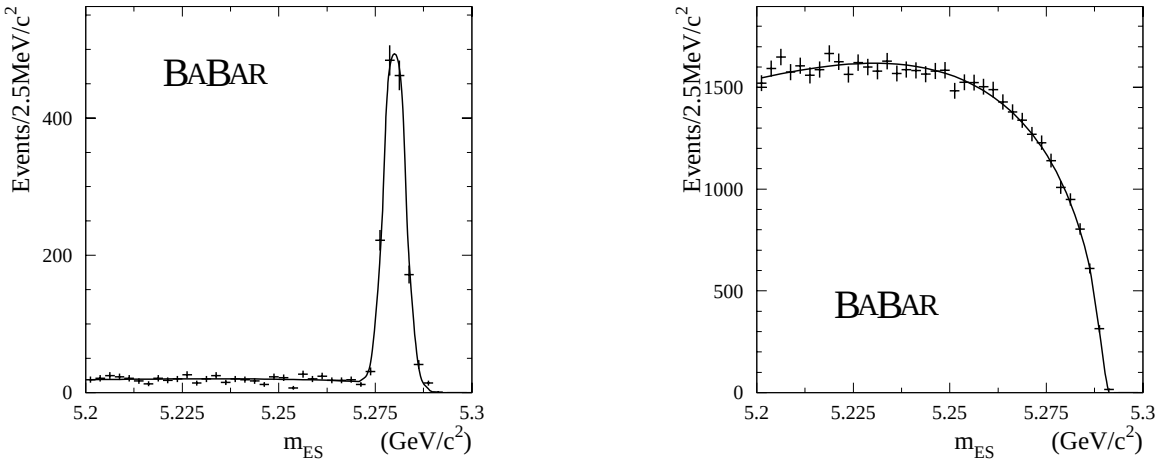

Figure 9: *m_{ES} distributions used to calibrate the m_{ES} PDF's. a) is from $B^- \to D^0(\to K^-\pi^+)\pi^-$ data and is used for the signal PDF. b) is from ΔE sideband data and is used for the background PDF.*

9.3 Calibration of PDF's

In order for the the fit to be valid, it is essential that the individual PDF's properly describe the distributions for the signal and background hypotheses. These PDF's are calculated based on calibration samples of real data and checked with Monte Carlo simulation. The following sections describe this procedure in more detail for each of the five fit variables.

9.3.1 m_{ES} PDF's

The shape of the m_{ES} distribution for signal is taken to be Gaussian. Since its width is dominated by the beam spread energy, it can be reliably calculated based on fully reconstructed decays of the type $B^- \to D^0(\to K^-\pi^+)\pi^-$. Figure 9(a) shows the shape of this distribution. For background, the shape is assumed to be the "Argus Function", which is fitted to data taken on the $\Upsilon(4s)$ peak, but with ΔE outside of the signal region. Figure 9(b) shows this distribution and its fit.

9.3.2 ΔE PDF's

The ΔE shape for signal is assumed to be Gaussian. In contrast to the m_{ES} case, however, the width is dominated by tracking resolution and is therefore different for $B^- \to D^0(\to K^-\pi^+)\pi^-$ than for $B^0 \to h^+h'^-$. In this case, we compare the width measured in data for $B^- \to D^0(\to K^-\pi^+)\pi^-$, $\sigma_{\Delta E} = 19MeV$, with that found in Monte Carlo, $\sigma_{\Delta E} = 15MeV$. We then scale up the width found in signal Monte Carlo ($\sigma_{\Delta E} = 21MeV$) by the same factor to obtain the width used for the PDF, $\sigma_{\Delta E} = 26 \pm 5MeV$. For background, the shape is taken to be a polynomial, which is fitted to data taken on peak, but outside of the ΔE signal region.

Decay Mode	$N_{signal} \pm \sigma_{stat} \pm \sigma_{syst}$	BR BABAR ($\times 10^{-6}$)
$\pi^+\pi^-$	$41 \pm 10 \pm 7$	$4.1 \pm 1.0 \pm 0.7$
$K^+\pi^-$	$169 \pm 17^{+12}_{-17}$	$16.7 \pm 1.6^{1.2}_{-1.7}$
K^+K^-	$8.2^{+7.8}_{-6.4} \pm 3.3$	< 2.5(90% C.L.)

Table 2: *Number of events for each mode found in the Maximum Likelihood Fit and the corresponding measured branching ratios.*

Parameter	Measurement
BR($B^0 \to K^{*0}\gamma$)	$(4.39 \pm 0.41 \pm 0.27) \times 10^{-5}$
$A_{CP}(B^0 \to K^{*0}\gamma)$	$-0.035 \pm 0.094 \pm 0.022$
BR($B^0 \to K^+\pi^-$)	$(16.7 \pm 1.6^{+1.2}_{-1.7}) \times 10^{-6}$
BR($B^0 \to \pi^+\pi^-$)	$(4.1 \pm 1.0 \pm 0.7) \times 10^{-6}$

Table 3: *Summary of measurement presented in this paper. In each case, the first error is statistical and the second s systematic.*

9.3.3 Fisher Discriminant PDF's

Double Gaussians are used for the Fisher discriminant shape. Signal Monte Carlo is used to determine the parameters for signal. It is checked with the $B^- \to D^0(\to K^-\pi^+)\pi^-$ sample. For background, the parameters are determined using the m_{ES} sideband and are checked using off-resonance data and continuum Monte Carlo.

9.3.4 θ_C PDF's

A sample of $D^{*+} \to \pi^+_{slow} D^0(D^0 \to K^-\pi^+)$ was used to provide clean samples of π^+'s and K^+'s. The DIRC θ_C response was parameterized by a Gaussian with mean and width dependent on dip angle. Also, it was necessary to include small non-Gaussian "satellite" peaks in order to adequately model the performance.

9.4 $B^0 \to h^+h'^-$ Fit Result

The maximum likelihood fit yields the results shown in Table 2. The systematic errors are calculated by varying the parameters of the PDF's, both within their statistical errors and to cover any disagreements between data and Monte Carlo. More information about this analysis may be found in [8].

10 Conclusions

Based on a first year sample of 22.4×10^6 $B\bar{B}$ pairs, BABAR has the preliminary measurements shown in Table 3. As more data is collected and more decays modes analyzed, BABAR will have many more results on charmless B decays.

References

[1] J. Hewett and J. Wells, P., *Phys. Rev.* D **55**, 5549 (1997).

[2] M. Gronau and D. London, *Phys. Rev. Let.* **65**, 3381 (1990).

[3] BABAR Collaboration, B. Auber *et al*, BABAR-CONF-00/15, submitted to the XXX^{th} ICHEP 2000, Osaka, Japan, 2000.

[4] BABAR Collaboration, B. Auber *et al*, BABAR-CONF-00/12, submitted to the XXX^{th} ICHEP 2000, Osaka, Japan, 2000.

[5] D.N. Brown, in these proceedings.

[6] B. Ratcliff, SLAC-PUB-5946 (1992), SLAC-PUB-6607 (1993); P. Coyle *et al*, *Nucl. Instr. & Meth.* **A343**, 292 (1993).

[7] CLEO Collaboration, A. Cronin-Hennesy *et al*, *Phys. Rev. Let.* **85**, 515 (2000).

[8] BABAR Collaboration, B. Aubert *et al*, "Measurement of Branching Fractions and Search for CP-Violating Charge Asymmetries in Charmless Two-Body B Decays into Pions and Kaons", hep-ex/0105061.